Finite-Size Spectral Signatures of Order by Quantum Disorder: A Perspective from Anderson's Tower of States

Subhankar Khatua,[1,2,3] Griffin C. Howson,[1,2] Michel J. P. Gingras,[1,4] and Jeffrey G. Rau[2]

[1]*Department of Physics and Astronomy, University of Waterloo, Waterloo, Ontario, N2L 3G1, Canada*
[2]*Department of Physics, University of Windsor, 401 Sunset Avenue, Windsor, Ontario, N9B 3P4, Canada*
[3]*Institute for Theoretical Solid State Physics, IFW Dresden and Würzburg-Dresden Cluster of Excellence ct.qmat, Helmholtzstr. 20, 01069 Dresden, Germany*
[4]*Waterloo Institute for Nanotechnology, University of Waterloo, Waterloo, Ontario, N2L 3G1, Canada*

(Dated: September 16, 2025)

In frustrated magnetic systems with a subextensive number of classical ground states, quantum zero-point fluctuations can select a unique long-range ordered state, a celebrated phenomenon referred to as *order by quantum disorder* (ObQD). For frustrated spin-$\frac{1}{2}$ systems, unbiased numerical methods able to expose ObQD are necessary. We show that ObQD can be identified from exact diagonalization (ED) calculations through an analysis akin to the Anderson tower of states associated with spontaneous symmetry breaking. By defining an effective quantum rotor model, we describe the competition between ObQD-induced localization of the rotor and its tunneling between symmetry-related ground states, identifying the crossover lengthscale from the finite-size regime where the rotor is delocalized, to the infinite system-size limit where it becomes localized. This rotor model relates the characteristic splittings in the ED energy spectrum to the ObQD selection energy scale, providing an estimate that can be compared to spin wave calculations. We demonstrate the general applicability of this approach in one-, two- and three-dimensional frustrated spin models that exhibit ObQD.

Many theoretical models of highly frustrated spin systems display an exponentially large manifold of accidentally degenerate classical ground states that is not a consequence of any global symmetry [1–6]. This extensive degeneracy may give rise to a spin liquid phase in which the spins remain fluctuating down to zero temperature [1, 4–8]. However, real frustrated magnetic materials generally possess additional small interactions that can lift such accidental classical ground state degeneracy, yielding a long-range ordered state, albeit with residual quantum fluctuations, and thus forestalling the formation of a spin liquid state [6, 9, 10].

Interestingly, an intermediate case is possible where, despite perturbing interactions, some degree of frustration persists, with the situation sitting between the two aforementioned extreme limits: instead of a unique ground state (up to global symmetries) or an exponentially large number of ground states, only a subextensive manifold of classical ground states remains. In such a scenario, quantum fluctuations may, perhaps counterintuitively, stabilize long-range magnetic order rather than prevent it—a phenomenon known as "order by quantum disorder" (ObQD) [11]. ObQD has drawn significant attention over the years, with many spin models having been found to exhibit this phenomenon [11–26] and some potential experimental realizations of ObQD in materials [27–33].

Linear spin wave theory (LSWT) [34, 35] has been the prevailing method for studying ObQD in frustrated spin models [11–25, 27–33]. This *semiclassical* formalism treats quantum fluctuations as a perturbation about a classically ordered state stabilized for large spin length S. The leading quantum correction to the energy is the zero-point energy (ZPE) of each classically degenerate ground state and the state with smallest ZPE is selected—order by quantum fluctuations (i.e. disorder). It remains an open question to what extent this approach can be applied to systems with smaller, more realistic values of S. A quantitative understanding of ObQD in spin-$\frac{1}{2}$ systems, of foremost interest to experimentalists and theorists alike, requires a fully quantum approach, not rooted in the semiclassical limit. Since exact analytical treatments are scarce for frustrated $S = \frac{1}{2}$ systems, numerical techniques are essential. While there exist many such methods, exact diagonalization (ED) is often the tool of choice [36, 37] as it is applicable to general spin models, provides access to the full spectrum, and can yield useful results in one, two, and even three dimensions. Other numerical approaches [36, 38–46]

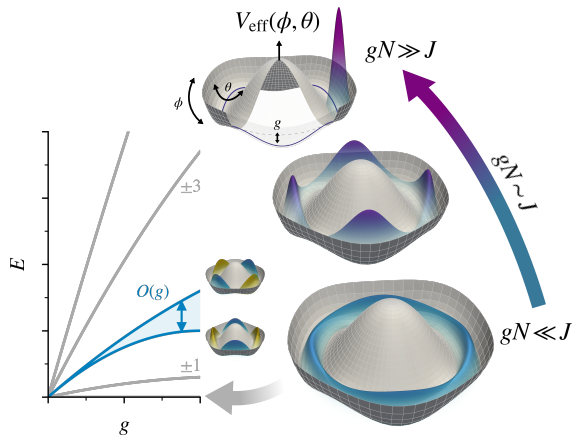

FIG. 1. Illustration of order by quantum disorder (ObQD) selection, with selection energy scale g, showing the evolution from the finite-size limit $gN \ll J$, to the thermodynamic limit $gN \gg J$ (where N is the number of spins). For small systems, tunneling delocalizes the order parameter across classical ground states, with ObQD acting as a small perturbation. (Inset) The scale of this perturbation can be read off the splittings of the excited states in the (approximate) Anderson tower of states. The order parameter localizes at the ObQD-selected state as $N \to \infty$.

fall short on one or more of these points, limiting their applicability in characterizing ObQD.

Unfortunately, being constrained to small system sizes, ED suffers from strong finite-size effects [36, 37]. Notwithstanding, this limitation can reveal valuable insights since the finite-size low-energy spectrum contains structure that reflects the underlying ordering mechanism. This is exemplified by the "Anderson tower of states", a hallmark of spontaneous symmetry breaking (SSB) in finite size systems [47–51]. The energy of the states in this tower scales inversely with system size (i.e., as $1/N$), collapsing into a degenerate set of states as $N \to \infty$, with the states that spontaneously break symmetry emerging as a superposition within this degenerate set. Despite its success in describing how SSB appears in finite-size spin-$\frac{1}{2}$ systems [50–57], there is no similar understanding for ObQD [22, 50, 58, 59]. This raises the fundamental and, to the best of our knowledge, unaddressed question—how does ObQD manifest in finite-size spin-$\frac{1}{2}$ systems and how is ObQD selection in the thermodynamic limit foreshadowed?

In this Letter, we identify signatures of ObQD in the low-energy spectrum of finite-size spin-$\frac{1}{2}$ systems and propose a prescriptive methodology for diagnosing ObQD in ED results. These signatures are encoded in a finite-size description of the order parameter dynamics based on an effective quantum rotor model extending the conventional Anderson tower of states framework. This rotor model reproduces the spectroscopic signatures observed in ED data and captures the interplay between ObQD-induced localization of the rotor and quantum tunneling among symmetry-related ground states (see Fig. 1). In particular, this framework exposes the crossover from the finite-size regime, where the rotor is delocalized over the quasi-degenerate manifold, to the thermodynamic limit, where it localizes and long-range order occurs. By exploiting the characteristic splittings identified in the ED spectrum, we extract the ObQD energy scale and argue that these splittings constitute the finite-size manifestation of the energy gap of the ObQD-induced pseudo-Goldstone (PG) mode [20]. We compare estimates of the ObQD energy scale from these $S = \frac{1}{2}$ calculations with semiclassical results for several paradigmatic ObQD models and find reasonable agreement. Finally, we discuss implications for the pyrochlore magnet $Er_2Ti_2O_7$, a leading candidate material for ObQD [30, 31].

Ferromagnetic Heisenberg-compass model.— We first consider the ferromagnetic Heisenberg-compass model on the square lattice [24, 60], relevant to spin-orbit Mott insulators [61]

$$\mathcal{H} = \sum_{\boldsymbol{r}} \Big[J \sum_{\boldsymbol{\delta}=\boldsymbol{x},\boldsymbol{y}} \boldsymbol{S}_{\boldsymbol{r}} \cdot \boldsymbol{S}_{\boldsymbol{r}+\boldsymbol{\delta}} + K \left(S^x_{\boldsymbol{r}} S^x_{\boldsymbol{r}+\boldsymbol{x}} + S^y_{\boldsymbol{r}} S^y_{\boldsymbol{r}+\boldsymbol{y}} \right) \Big], \quad (1)$$

where $\boldsymbol{S}_{\boldsymbol{r}} \equiv \left(S^x_{\boldsymbol{r}}, S^y_{\boldsymbol{r}}, S^z_{\boldsymbol{r}} \right)$ is a spin-$\frac{1}{2}$ operator at lattice site $\boldsymbol{r}$, and $\boldsymbol{\delta} = \boldsymbol{x}, \boldsymbol{y}$ are the nearest-neighbor bonds. The first and second terms in Eq. (1) are the nearest-neighbor Heisenberg and bond-dependent compass exchanges, respectively. We parametrize $J \equiv \cos\xi$ and $K \equiv \sin\xi$ with $\pi < \xi < 3\pi/2$ where both couplings are ferromagnetic (i.e., negative). The compass term breaks the SU(2) spin-rotation symmetry of the Heisenberg term, reducing the symmetry to discrete C_{4z} and C_{2x}, C_{2y} operations.

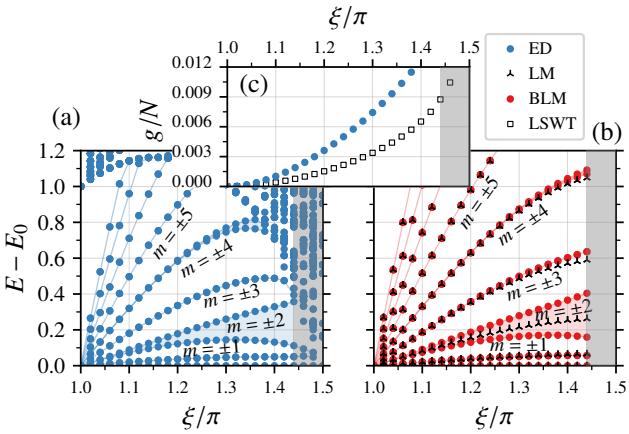

FIG. 2. Ferromagnetic Heisenberg-compass model on the square lattice of $N = 16$ sites with periodic boundary conditions. (a) Low-energy ED spectrum. The m labels correspond to the unsplit rotor energy levels, with the splitting of the $m = \pm 2$ and $m = \pm 4$ levels emphasized by light blue shaded wedges. The lines are guides to the eye. (b) Spectrum of the LM and BLM models, where the g value for the BLM description is extracted from the splitting in the ED spectrum. (c) Comparison of the ObQD energy scale, g, obtained from finite-size LSWT for $N = 16$ and ED data. Grey areas in all panels mark deviations from the BLM picture due to a new phase near $\xi = 3\pi/2$ [24].

ObQD in this model has been previously studied using LSWT [20, 24, 60]. In the classical limit ($S \to \infty$), the ground states are ferromagnetic configurations aligned along *any* direction in the $\hat{\boldsymbol{x}} - \hat{\boldsymbol{y}}$ plane, forming an accidentally degenerate continuous O(2) manifold. Spin-wave zero-point fluctuations lift this degeneracy, yielding ObQD for states aligned along $\pm\hat{\boldsymbol{x}}$, $\pm\hat{\boldsymbol{y}}$ directions [20, 24]. To assess the extent to which the semiclassical understanding of ObQD carries over to the $S = \frac{1}{2}$ limit, we perform ED, exploiting the discrete translational symmetry of the model to obtain the low-energy spectrum shown in Fig. 2(a). Since for small system sizes, the ED ground state shows only a very weak preference for ObQD-selected orderings [24], we look beyond the ground state to the excited states.

Do the excited states reveal signatures of ObQD? Specifically, is there any underlying structure in the spectrum connected to the ObQD observed in the thermodynamic limit? This question is reminiscent of the related challenge in identifying SSB in finite-size systems [47, 50, 51]. To proceed, we formulate an effective description of ObQD based on the Lieb-Mattis (LM) framework [62], previously used to understand finite-size signatures of SSB—namely, the Anderson tower of states [47–51]. The LM Hamiltonian can be derived by projecting the full Hamiltonian [Eq. (1)] into its lowest-energy subspace [59, 63]: the ferromagnetic sector with total spin $S_{\text{tot}} = \frac{N}{2}$, where N is the total number of spins. This yields an effective Hamiltonian in terms of a single large spin of length S_{tot}: $\mathcal{H}_{\text{LM}} = -K(S^z_{\text{tot}})^2/(N-1)$ [64] where S^z_{tot} has eigenvalues

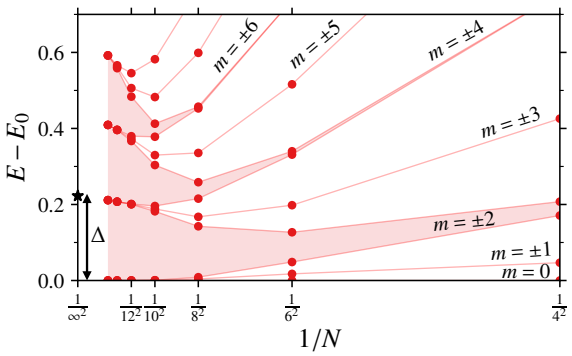

FIG. 3. Finite size scaling of the BLM spectrum of the Heisenberg-compass model with $\xi = 5\pi/4$. The g value for the BLM model is determined from LSWT on an N-site lattice. Lines are guides to the eye, tracking the scaling of the energy eigenvalues. Shaded areas show ObQD-induced splitting. Black star marker is the system size extrapolated value of the gap Δ from the ground state to the first excited state reproducing the pseudo-Goldstone gap [20].

$m = 0, \pm 1, \cdots, \pm S_{\text{tot}}$ [65]. This is a planar quantum rotor with moment of inertia $I = (N-1)/(2|K|)$ that increases with system size. Since $K < 0$, the ground state has $m = 0$, while the excited states are each doubly degenerate with $|m| = 1, 2, \ldots, S_{\text{tot}}$ [see Fig. 2(b)].

Comparing this with the ED spectrum in Fig. 2(a), we find a good qualitative agreement, *except* for splittings visible in several excited doublets as ξ (i.e., $|K|$) increases. While the LM rotor predicts doublets for the $m = \pm 2$ and $m = \pm 4$ energy levels, the ED data in Fig. 2(a) shows this degeneracy is lifted. This discrepancy arises because $\mathcal{H}_{\text{LM}}$ possesses a U(1) symmetry about the $\hat{\boldsymbol{z}}$ axis while the microscopic spin Hamiltonian [Eq. (1)] does not. This symmetry of $\mathcal{H}_{\text{LM}}$ reflects the accidental degeneracy of the classical ground states and, despite forming the foundation of the effective theory of SSB, $\mathcal{H}_{\text{LM}}$ is unable to capture ObQD.

Beyond the Lieb-Mattis model.— To account for ObQD, it is thus necessary to go beyond the LM projection by breaking the emergent U(1) symmetry and restoring the discrete symmetries of the full Hamiltonian [59]. Such corrections can in principle be derived via second-order perturbation theory starting from the isotropic LM limit [59], however such calculations are challenging for Hamiltonians without continuous spin-rotation symmetry [66].

We therefore take a simpler alternative route: we introduce the U(1) breaking term phenomenologically, inspired by spin-wave theory. In LSWT, the term that restores the discrete symmetries is the spin-wave ZPE, of the form $-g\cos(4\phi)$ [24], where ϕ is the moment orientation of the ferromagnetic ground states relative to $\hat{\boldsymbol{x}}$ and the parameter g is the ObQD energy scale. We thus promote this ZPE to an operator [65]

$$\mathcal{H}_{\text{pert}} = -\frac{g}{2}\frac{\left[(S^+_{\text{tot}})^4 + (S^-_{\text{tot}})^4\right]}{\left[N/2(N/2+1)\right]^2}, \tag{2}$$

where $S^{\pm}_{\text{tot}}$ are the raising and lowering operators in the $S_{\text{tot}} = \frac{N}{2}$ space and the denominator accounts for the length of $\boldsymbol{S}_{\text{tot}}$, i.e., $\sqrt{N/2(N/2+1)}$ [67]. This minimal term embeds ObQD in the effective description, with g a phenomenological parameter setting the energy scale of the ground state selection [68].

The resulting "beyond Lieb-Mattis" (BLM) Hamiltonian, $\mathcal{H}_{\text{BLM}} \equiv \mathcal{H}_{\text{LM}} + \mathcal{H}_{\text{pert}}$, describes the motion of the rotor in an ObQD-induced "potential", $\mathcal{H}_{\text{pert}}$, with minima along $\pm\hat{\boldsymbol{x}}, \pm\hat{\boldsymbol{y}}$ directions. The effect of this potential on the spectrum of $\mathcal{H}_{\text{BLM}}$ can be understood by treating $\mathcal{H}_{\text{pert}}$ as a perturbation to $\mathcal{H}_{\text{LM}}$, since g is an extensive quantity (i.e., $\propto N$) and therefore weaker for small system sizes. Due to the quartic dependence of $\mathcal{H}_{\text{pert}}$ on $S^{\pm}_{\text{tot}}$, degenerate states with $\Delta m = \pm 4$ split at first order in g, while those with $\Delta m = \pm 8$ split at second order. The $m = \pm 1, \pm 3, \ldots$ states thus remain degenerate, while the $m = \pm 2$ and $m = \pm 4$ states exhibit splittings of $O(g)$ and $O(g^2)$, respectively—the latter being much smaller.

These splittings relate the BLM and ED spectra. Focusing on the $m = \pm 2$ states, the BLM splitting, Δ, is given perturbatively by $\Delta = \frac{(N/2-1)(N/2+2)}{N/2(N/2+1)}g$ [65]. We can then use the same splitting from the ED spectrum, Δ_{ED}, and equate $\Delta = \Delta_{\text{ED}}$ to produce an estimate for the value of g from the microscopic model. A comparison of the ED spectrum [Fig. 2(a)] and BLM spectrum using the extracted values of g [Fig. 2(b)] reveals compelling qualitative agreement [69]. This BLM description exposes that the pattern of splittings observed in the excited energy levels in the ED spectrum *originates* from the physics of ObQD, further providing an estimate of the ObQD energy scale—this is the key result of this paper.

As the energy scale g was motivated by the form of the ObQD potential that appears in LSWT, it can be directly compared to the semiclassical value computed as half of the ZPE difference between the $\phi = \frac{\pi}{4}$ and $\phi = 0$ states. As shown in Fig. 2(c), there is qualitative agreement—about a factor of two—between the value of g extracted from ED, g_{ED}, and the value of g directly computed from LSWT, g_{LSWT}.

The BLM Hamiltonian has two important limits: for smaller systems, the kinetic rotor term ($\mathcal{H}_{\text{LM}}$) dominates over the ObQD-induced potential as its moment of inertia scales as $\propto (N-1)$; the rotor remains delocalized in the $\hat{\boldsymbol{x}} - \hat{\boldsymbol{y}}$ plane, hybridizing among the accidentally degenerate ground states. In the opposite limit of larger systems, the potential dominates, localizing the rotor near the potential minima and suppressing the tunneling through the potential barriers (see Fig. 1). The crossover between these two limits can be seen in the finite-size scaling of the BLM spectrum at a fixed ξ, as shown in Fig. 3 for a BLM model where here we have set $g = g_{\text{LSWT}}$. Groups of four states converge as N increases, becoming quasi-degenerate for sufficiently large systems, consistent with the semiclassical picture of ObQD selecting four states in the thermodynamic limit. The near-degeneracy of the lowest four states at $N^* \approx 64$ marks the crossover from rotor-dominated to ObQD-dominated physics [see Fig. 1]. In the large-N limit, the energy gap Δ to the first excited state shown in Fig. 3 approaches the ObQD-induced PG gap determined from LSWT [20]. The precise agreement of the PG gap from the two approaches in the large-N limit is by construction, due to g being fixed using LSWT. Thus, the BLM description offers a clear picture of the mechanism by which

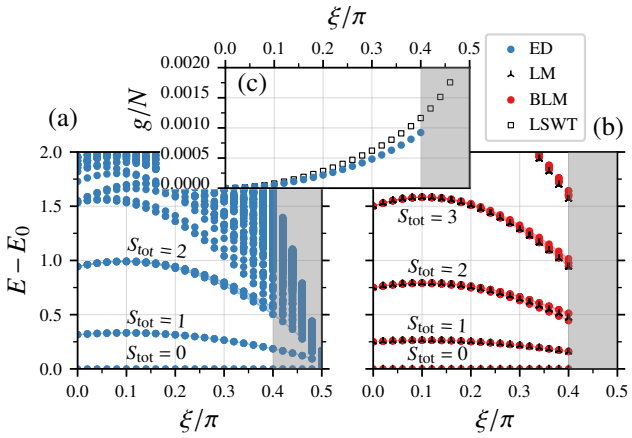

FIG. 4. Antiferromagnetic Heisenberg-Kitaev model on the honeycomb lattice of $N = 24$ sites with periodic boundary conditions. a) Low-energy ED spectrum. (b) Spectra of the LM and BLM models, where the g value for the BLM description is extracted from the splitting in ED spectrum. (c) g obtained from LSWT and the ED spectrum. Grey areas in all panels mark the regime where the low-energy physics begins to deviate from the BLM description as it approaches the Kitaev quantum spin liquid phase near $\xi = \pi/2$ [70].

ObQD operates in spin-$\frac{1}{2}$ systems, from finite-size clusters to the thermodynamic limit.

Interestingly, this Heisenberg-compass model also exhibits ObQD in the antiferromagnetic regime (i.e., $J > 0$, $K > 0$), but now into Néel order along the $\pm\hat{\boldsymbol{x}}, \pm\hat{\boldsymbol{y}}$ directions [24]. A direct application of the BLM framework yields a similar effective rotor physics in the finite-size spin-$\frac{1}{2}$ limit (see Supplemental Material (SM) [65]).

Antiferromagnetic Heisenberg-Kitaev model.— To demonstrate the broad applicability of this framework, we consider another model, the Heisenberg-Kitaev model on the honeycomb lattice [70–72] relevant to candidate Kitaev materials [10, 70, 71], that yields qualitatively different rotor physics. The Hamiltonian is $\mathcal{H} = \sum_{\langle \boldsymbol{r}\boldsymbol{r}'\rangle \in \gamma} \left[J \boldsymbol{S}_{\boldsymbol{r}} \cdot \boldsymbol{S}_{\boldsymbol{r}'} + K S^{\gamma}_{\boldsymbol{r}} S^{\gamma}_{\boldsymbol{r}'} \right]$, where J, K are the Heisenberg and Kitaev couplings, respectively, and $\gamma = x, y, z$ labels the three types of nearest-neighbor bonds. The bond-dependent Kitaev interaction breaks SU(2) spin-rotation symmetry of the Heisenberg term down to discrete symmetries [65].

For $J > 0$ and $K > 0$, classical ground states are accidentally degenerate Néel states with arbitrary orientation, and ObQD selects those along $\pm\hat{\boldsymbol{x}}, \pm\hat{\boldsymbol{y}}, \pm\hat{\boldsymbol{z}}$ directions [20, 70, 71]. The low-energy $S = \frac{1}{2}$ ED spectrum is shown in Fig. 4(a) with $J \equiv \cos\xi$ and $K \equiv \sin\xi$ for $0 < \xi < \pi/2$. To identify signatures of ObQD in this spectrum, we follow the same procedure as laid out above for the ferromagnetic Heisenberg-compass model.

Unlike an effective spin of length $N/2$ describing the ferromagnetic subspace, the relevant low-energy subspace now consists of two large spins of length $N/4$, corresponding to the two sublattices A and B of the Néel ordering, each containing $N/2$ spins. The resulting LM Hamiltonian is $\mathcal{H}_{\rm LM} = \frac{3J+K}{N}(\boldsymbol{S}^2_{\rm tot} - \boldsymbol{S}^2_A - \boldsymbol{S}^2_B)$ [65], where $\boldsymbol{S}_{\rm tot} = \boldsymbol{S}_{\rm A} + \boldsymbol{S}_{\rm B}$. Since $\mathcal{H}_{\rm LM}$ has SU(2) symmetry, $S_{\rm tot}$ and $S^z_{\rm tot}$ are conserved. The ground state has $S_{\rm tot} = 0$, while excited states are labeled by $S_{\rm tot} = 1, 2, \ldots$, each with degeneracy $(2S_{\rm tot} + 1)$ [see Fig. 4(b)]. This qualitatively agrees with the ED spectrum [Fig. 4(a)], *except* for the splitting of the $S_{\rm tot} = 2$ level and above observed in the ED spectrum.

To resolve this discrepancy, we consider the BLM description, adding the operator equivalent of the spin-wave ZPE, as done previously. Here, the ZPE manifests as a cubic anisotropy, with minima along the $\pm\hat{\boldsymbol{x}}$, $\pm\hat{\boldsymbol{y}}$, $\pm\hat{\boldsymbol{z}}$ directions. The corresponding operator is [65]

$$\mathcal{H}_{\rm pert} = -g \frac{(S^x_A - S^x_B)^4 + (S^y_A - S^y_B)^4 + (S^z_A - S^z_B)^4}{[N/4(N/4+1)]^2}, \qquad (3)$$

where the denominator arises from the length of each effective large spin. The perturbative action of $\mathcal{H}_{\rm pert}$ on $\mathcal{H}_{\rm LM}$ mirrors the problem of a magnetic ion placed in a cubic crystal field environment [73]. It does not lift the degeneracy of the $S_{\rm tot} = 1$ level but splits the $S_{\rm tot} = 2$ level into the analogue of the e_g doublet and t_{2g} triplet [73], as clearly observed in both the ED [Fig. 4(a)] and BLM spectra [Fig. 4(b)]. Moreover, g from LSWT agrees well with that extracted from the $S_{\rm tot} = 2$ splitting in the ED spectrum [Fig. 4(c)]. The disagreement between the BLM and ED spectra near $\xi = \pi/2$ arises due to the presence of the Kitaev spin liquid phase in this region [70]. The ferromagnetic counterpart of this model (i.e., $J < 0$, $K < 0$) also exhibits ObQD [70, 71], with the BLM framework again yielding an analogous rotor description in the finite-size spin-$\frac{1}{2}$ limit (details in SM [65]). A one-dimensional version of the ferromagnetic Heisenberg-Kitaev model also exhibits ObQD [74], and its effective rotor physics can be obtained by a straightforward application of the BLM framework, as discussed in SM [65].

Conclusion.— To date, an understanding of the mechanism for order by quantum disorder (ObQD) has been lacking in finite-size $S = \frac{1}{2}$ systems. We have considered two textbook models harboring ObQD and presented an effective beyond Lieb-Mattis (BLM) description of how ObQD operates in the spin-$\frac{1}{2}$ limit, from finite-size systems to the thermodynamic limit. We identified a pattern of splittings in the *excited states* in the low-energy exact diagonalization (ED) spectrum, serving as a precursor to ObQD in the thermodynamic limit. Just as the Anderson tower of states serves as a diagnostic of spontaneous symmetry breaking in finite-size spin-$\frac{1}{2}$ systems, our analysis plays a similar role for ObQD.

The effective BLM description captures the crossover from a delocalized rotor in small systems to ObQD-dominated localized rotor in larger systems. This crossover can occur at system sizes significantly larger than those typically accessible to most unbiased numerical techniques. For example, in the ferromagnetic Heisenberg-compass model on the square lattice, it appears around $N^* \approx 64$. The value of N^* depends on the model and may be much larger in systems with weaker ObQD-selection effects. Only if ED calculations were feasible for such sizes would one observe a clear signature of ObQD-induced ordering in the ground state.

Our effective framework is general, applicable to any model exhibiting ObQD in one, two, or three dimensions, with no restrictions on symmetry or lattice type. We have demonstrated this generality via canonical two-dimensional examples, as well as a one-dimensional example [65]. We have also applied our framework to a three-dimensional case, $Er_2Ti_2O_7$, a preeminent candidate material for ObQD (see End Matter A). This pyrochlore magnet of effective spins ($S = \frac{1}{2}$) orders into a non-collinear "ψ_2" state [30, 31]. We find signatures of ObQD in its ED spectrum, with qualitative agreement between the ObQD energy scale g extracted from the splittings and LSWT.

The finite-size spectroscopic analysis of ObQD presented in this work reveals not only the selected ordering, but also the strength of the selection, which is roughly within a factor of two of its value in the thermodynamic limit for all the models we examined. Similar finite-size spectroscopic approaches have also proven successful in exposing the physics arising in the thermodynamic limit in other contexts including quantum criticality [75–79] and quantum spin liquids [75, 76, 79]. We believe our work significantly deepens the understanding of order by disorder in the finite-size and extreme $S = \frac{1}{2}$ quantum limit. We hope it encourages further exploration of finite-size quantum spectra as a diagnostic tool for uncovering emergent order, and inspires new directions in the study of fluctuation-driven phenomena in frustrated quantum magnets.

Acknowledgments—We thank Alex Hickey, Andreas Läuchli, Natalia Perkins, and Ioannis Rousochatzakis for discussions. The work at U. of Waterloo and U. of Windsor was funded by the NSERC of Canada (M.J.P.G, J.G.R) and the Canada Research Chair Program (M.J.P.G, Tier I). S. K. acknowledges financial support from the Deutsche Forschungsgemeinschaft (DFG, German Research Foundation) under Germany's Excellence Strategy through the Hallwachs-Röntgen Postdoc Program of the Würzburg-Dresden Cluster of Excellence on Complexity and Topology in Quantum Matter - ct.qmat (EXC 2147, project-id 390858490) and thanks Ulrike Nitzsche for technical assistance. G.C.H. acknowledges funding from the NSERC of Canada through the USRA and CGS-M programs. This research was supported in part by grant NSF PHY-1748958 to the Kavli Institute for Theoretical Physics (KITP).

[1] P. W. Anderson, Ordering and antiferromagnetism in ferrites, Phys. Rev. **102**, 1008 (1956).
[2] J. Villain, Insulating spin glasses, Zeitschrift für Physik B Condensed Matter **33**, 31 (1979).
[3] J. T. Chalker, P. C. W. Holdsworth, and E. F. Shender, Hidden order in a frustrated system: Properties of the Heisenberg kagomé antiferromagnet, Phys. Rev. Lett. **68**, 855 (1992).
[4] R. Moessner and J. T. Chalker, Low-temperature properties of classical geometrically frustrated antiferromagnets, Phys. Rev. B **58**, 12049 (1998).
[5] S. T. Bramwell and M. J. P. Gingras, Spin ice state in frustrated magnetic pyrochlore materials, Science **294**, 1495 (2001).
[6] L. Balents, Spin liquids in frustrated magnets, Nature **464**, 199 (2010).
[7] M. J. P. Gingras and P. A. McClarty, Quantum spin ice: a search for gapless quantum spin liquids in pyrochlore magnets, Reports on Progress in Physics **77**, 056501 (2014).
[8] L. Savary and L. Balents, Quantum spin liquids: a review, Reports on Progress in Physics **80**, 016502 (2017).
[9] C. Lacroix, P. Mendels, and F. M. (eds.), *Introduction to Frustrated Magnetism: Materials, Experiments, Theory* (Springer Berlin, 2011).
[10] S. Trebst and C. Hickey, Kitaev materials, Physics Reports **950**, 1 (2022).
[11] E. F. Shender, Antiferromagnetic garnets with fluctuationally interacting sublattices, Sov. Phys. JETP **56**, 178 (1982).
[12] E. Rastelli and A. Tassi, Order produced by quantum disorder in the Heisenberg rhombohedral antiferromagnet, Journal of Physics C: Solid State Physics **20**, L303 (1987).
[13] C. L. Henley, Ordering due to disorder in a frustrated vector antiferromagnet, Phys. Rev. Lett. **62**, 2056 (1989).
[14] J. R. Tessman, Magnetic anisotropy at 0°K, Phys. Rev. **96**, 1192 (1954).
[15] K. Kubo and T. Kishi, Ordering due to quantum fluctuations in the frustrated Heisenberg model, Journal of the Physical Society of Japan **60**, 567 (1991).
[16] A. Chubukov, Order from disorder in a kagomé antiferromagnet, Phys. Rev. Lett. **69**, 832 (1992).
[17] C. L. Henley, Selection by quantum fluctuations of dipolar order in a diamond lattice, Phys. Rev. Lett. **73**, 2788 (1994).
[18] P. A. McClarty, P. Stasiak, and M. J. P. Gingras, Order-by-disorder in the XY pyrochlore antiferromagnet, Phys. Rev. B **89**, 024425 (2014).
[19] B. Danu, G. Nambiar, and R. Ganesh, Extended degeneracy and order by disorder in the square lattice $J_1 - J_2 - J_3$ model, Phys. Rev. B **94**, 094438 (2016).
[20] J. G. Rau, P. A. McClarty, and R. Moessner, Pseudo-Goldstone gaps and order-by-quantum disorder in frustrated magnets, Phys. Rev. Lett. **121**, 237201 (2018).
[21] R. Schick, T. Ziman, and M. E. Zhitomirsky, Quantum versus thermal fluctuations in the fcc antiferromagnet: Alternative routes to order by disorder, Phys. Rev. B **102**, 220405 (2020).
[22] S. Khatua, S. Srinivasan, and R. Ganesh, State selection in frustrated magnets, Phys. Rev. B **103**, 174412 (2021).
[23] V. Noculak, D. Lozano-Gómez, J. Oitmaa, R. R. P. Singh, Y. Iqbal, M. J. P. Gingras, and J. Reuther, Classical and quantum phases of the pyrochlore $s = \frac{1}{2}$ magnet with Heisenberg and Dzyaloshinskii-Moriya interactions, Phys. Rev. B **107**, 214414 (2023).
[24] S. Khatua, G. C. Howson, M. J. P. Gingras, and J. G. Rau, Ground state properties of the Heisenberg-compass model on the square lattice, Phys. Rev. B **110**, 104426 (2024).
[25] A. Hickey, D. Lozano-Gómez, and M. J. P. Gingras, Order-by-disorder without quantum zero-point fluctuations in the pyrochlore Heisenberg ferromagnet with Dzyaloshinskii-Moriya interactions, Phys. Rev. B **111**, 184434 (2025).
[26] A. Hickey, J. G. Rau, S. Khatua, and M. J. P. Gingras, Universal temperature-dependent power law excitation gaps in frustrated quantum spin systems harboring order-by-disorder (2025), arXiv:2505.18253 [cond-mat.str-el].

[27] T. Brueckel, B. Dorner, A. G. Gukasov, V. P. Plakhty, W. Prandl, E. F. Shender, and O. P. Smirnow, Dynamical interaction of antiferromagnetic subsystems: a neutron scattering study of the spinwave spectrum of the garnet $Fe_2Ca_3(GeO_4)_3$, Zeitschrift für Physik B Condensed Matter **72**, 477 (1988).

[28] Y. J. Kim, A. Aharony, R. J. Birgeneau, F. C. Chou, O. Entin-Wohlman, R. W. Erwin, M. Greven, A. B. Harris, M. A. Kastner, I. Y. Korenblit, Y. S. Lee, and G. Shirane, Ordering due to quantum fluctuations in $Sr_2Cu_3O_4Cl_2$, Phys. Rev. Lett. **83**, 852 (1999).

[29] J. D. M. Champion, M. J. Harris, P. C. W. Holdsworth, A. S. Wills, G. Balakrishnan, S. T. Bramwell, E. Čižmár, T. Fennell, J. S. Gardner, J. Lago, D. F. McMorrow, M. Orendáč, A. Orendáčová, D. M. Paul, R. I. Smith, M. T. F. Telling, and A. Wildes, $Er_2Ti_2O_7$: Evidence of quantum order by disorder in a frustrated antiferromagnet, Phys. Rev. B **68**, 020401 (2003).

[30] L. Savary, K. A. Ross, B. D. Gaulin, J. P. C. Ruff, and L. Balents, Order by quantum disorder in $Er_2Ti_2O_7$, Phys. Rev. Lett. **109**, 167201 (2012).

[31] K. A. Ross, Y. Qiu, J. R. D. Copley, H. A. Dabkowska, and B. D. Gaulin, Order by disorder spin wave gap in the *XY* pyrochlore magnet $Er_2Ti_2O_7$, Phys. Rev. Lett. **112**, 057201 (2014).

[32] C. L. Sarkis, J. G. Rau, L. D. Sanjeewa, M. Powell, J. Kolis, J. Marbey, S. Hill, J. A. Rodriguez-Rivera, H. S. Nair, D. R. Yahne, S. Säubert, M. J. P. Gingras, and K. A. Ross, Unravelling competing microscopic interactions at a phase boundary: A single-crystal study of the metastable antiferromagnetic pyrochlore $Yb_2Ge_2O_7$, Phys. Rev. B **102**, 134418 (2020).

[33] M. Elliot, P. A. McClarty, D. Prabhakaran, R. D. Johnson, H. C. Walker, P. Manuel, and R. Coldea, Order-by-disorder from bond-dependent exchange and intensity signature of nodal quasiparticles in a honeycomb cobaltate, Nature Communications **12**, 3936 (2021).

[34] T. Holstein and H. Primakoff, Field dependence of the intrinsic domain magnetization of a ferromagnet, Phys. Rev. **58**, 1098 (1940).

[35] A. Auerbach, *Interacting Electrons and Quantum Magnetism*, Graduate Texts in Contemporary Physics (Springer New York, 1998).

[36] A. W. Sandvik, Computational Studies of Quantum Spin Systems, AIP Conference Proceedings **1297**, 135 (2010).

[37] A. M. Läuchli, Numerical simulations of frustrated systems, in *Introduction to Frustrated Magnetism: Materials, Experiments, Theory*, edited by C. Lacroix, P. Mendels, and F. Mila (Springer Berlin Heidelberg, Berlin, Heidelberg, 2011) pp. 481–511.

[38] A. W. Sandvik and J. Kurkijärvi, Quantum Monte Carlo simulation method for spin systems, Phys. Rev. B **43**, 5950 (1991).

[39] O. F. Syljuåsen and A. W. Sandvik, Quantum Monte Carlo with directed loops, Phys. Rev. E **66**, 046701 (2002).

[40] N. Kawashima and K. Harada, Recent Developments of World-Line Monte Carlo Methods, J. Phys. Soc. Jpn. **73**, 1379 (2004).

[41] F. F. Assaad, M. Bercx, F. Goth, A. Götz, J. S. Hofmann, E. Huffman, Z. Liu, F. P. Toldin, J. S. E. Portela, and J. Schwab, The ALF (Algorithms for Lattice Fermions) project release 2.0. Documentation for the auxiliary-field quantum Monte Carlo code, SciPost Phys. Codebases , 1 (2022).

[42] S. R. White, Density matrix formulation for quantum renormalization groups, Phys. Rev. Lett. **69**, 2863 (1992).

[43] U. Schollwöck, The density-matrix renormalization group in the age of matrix product states, Annals of Physics **326**, 96 (2011), January 2011 Special Issue.

[44] F. Verstraete, V. Murg, and J. Cirac, Matrix product states, projected entangled pair states, and variational renormalization group methods for quantum spin systems, Advances in Physics **57**, 143 (2008).

[45] M. Rigol, T. Bryant, and R. R. P. Singh, Numerical Linked-Cluster Approach to Quantum Lattice Models, Phys. Rev. Lett. **97**, 187202 (2006).

[46] B. Tang, E. Khatami, and M. Rigol, A short introduction to numerical linked-cluster expansions, Comput. Phys. Commun. **184**, 557 (2013).

[47] P. W. Anderson, An approximate quantum theory of the antiferromagnetic ground state, Phys. Rev. **86**, 694 (1952).

[48] P. W. Anderson, *Concepts in Solids* (World Scientific, New Jersey, 1997).

[49] P. W. Anderson, *Basic Notions of Condensed Matter Physics* (CRC Press, 2018).

[50] C. Lhuillier, Frustrated quantum magnets (2005), arXiv:cond-mat/0502464 [cond-mat.str-el].

[51] A. Wietek, M. Schuler, and A. M. Läuchli, Studying continuous symmetry breaking using energy level spectroscopy (2017), arXiv:1704.08622 [cond-mat.str-el].

[52] H. Neuberger and T. Ziman, Finite-size effects in heisenberg antiferromagnets, Phys. Rev. B **39**, 2608 (1989).

[53] B. Bernu, C. Lhuillier, and L. Pierre, Signature of Néel order in exact spectra of quantum antiferromagnets on finite lattices, Phys. Rev. Lett. **69**, 2590 (1992).

[54] P. Hasenfratz and F. Niedermayer, Finite size and temperature effects in the AF Heisenberg model, Zeitschrift für Physik B Condensed Matter **92**, 91 (1993).

[55] P. Azaria, B. Delamotte, and D. Mouhanna, Spontaneous symmetry breaking in quantum frustrated antiferromagnets, Phys. Rev. Lett. **70**, 2483 (1993).

[56] B. Bernu, P. Lecheminant, C. Lhuillier, and L. Pierre, Exact spectra, spin susceptibilities, and order parameter of the quantum Heisenberg antiferromagnet on the triangular lattice, Phys. Rev. B **50**, 10048 (1994).

[57] J. B. Fouet, P. Sindzingre, and C. Lhuillier, An investigation of the quantum $J_1 - J_2 - J_3$ model on the honeycomb lattice, The European Physical Journal B - Condensed Matter and Complex Systems **20**, 241 (2001).

[58] P. Lecheminant, B. Bernu, C. Lhuillier, and L. Pierre, J_1-J_2 quantum Heisenberg antiferromagnet on the triangular lattice: A group-symmetry analysis of order by disorder, Phys. Rev. B **52**, 6647 (1995).

[59] N.-G. Zhang, C. L. Henley, C. Rischel, and K. Lefmann, Effective Hamiltonian and low-lying eigenenergy clustering patterns of four-sublattice antiferromagnets, Phys. Rev. B **65**, 064427 (2002).

[60] S. Khatua, M. J. P. Gingras, and J. G. Rau, Pseudo-Goldstone modes and dynamical gap generation from order by thermal disorder, Phys. Rev. Lett. **130**, 266702 (2023).

[61] Z. Nussinov and J. van den Brink, Compass models: Theory and physical motivations, Rev. Mod. Phys. **87**, 1 (2015).

[62] E. Lieb and D. Mattis, Ordering energy levels of interacting spin systems, Journal of Mathematical Physics **3**, 749 (1962).

[63] T. Roscilde, T. Comparin, and F. Mezzacapo, Rotor/spin-wave theory for quantum spin models with u(1) symmetry, Phys. Rev. B **108**, 155130 (2023).

[64] The $(N-1)$ denominator comes from the total number of interaction pairs per spin in this fully symmetric (maximum-spin) subspace.

[65] See Supplemental Material at [The link will be provided by the editor] for the details of the effective Lieb-Mattis and beyond-Lieb-Mattis model derivations. It also includes Refs. [20, 22, 24, 50, 51, 59, 62, 63, 66, 70, 71, 73, 74, 80–85].

[66] E. Liviotti, S. Carretta, and G. Amoretti, S-mixing contributions to the high-order anisotropy terms in the effective spin Hamil-

tonian for magnetic clusters, The Journal of Chemical Physics **117**, 3361 (2002).

[67] The factor $[N/2(N/2+1)]^2$ is a phenomenological normalization constant. The true N dependence could in principle be found from high-order many-body perturbation theory starting from the Heisenberg limit. This is computationally challenging for anisotropic Hamiltonians [66] and beyond the scope of this work.

[68] For the same reason that this accidental degeneracy cannot be lifted classically by two-spin interaction terms, the correction to $\mathcal{H}_{\mathrm{LM}}$ needed to explain the ObQD splittings must be a higher-spin operator.

[69] The disagreement near $\xi \sim 1.5\pi$ is due to a nearby competing phase [24] rendering the effective BLM description inapplicable.

[70] J. Chaloupka, G. Jackeli, and G. Khaliullin, Zigzag magnetic order in the iridium oxide Na_2IrO_3, Phys. Rev. Lett. **110**, 097204 (2013).

[71] J. Chaloupka, G. Jackeli, and G. Khaliullin, Kitaev-Heisenberg model on a honeycomb lattice: Possible exotic phases in iridium oxides A_2IrO_3, Phys. Rev. Lett. **105**, 027204 (2010).

[72] J. G. Rau, E. K.-H. Lee, and H.-Y. Kee, Spin-orbit physics giving rise to novel phases in correlated systems: Iridates and related materials, Annual Review of Condensed Matter Physics **7**, 195 (2016).

[73] P. Fazekas, *Lecture Notes on Electron Correlation and Magnetism* (World Scientific, New Jersey, 1999).

[74] W. Yang, C. Xu, S. Ma, A. Nocera, and I. Affleck, Left-left-right-right magnetic order in spin-$\frac{1}{2}$ Kitaev-Heisenberg chain, Phys. Rev. B **112**, 035104 (2025).

[75] M. Schuler, S. Whitsitt, L.-P. Henry, S. Sachdev, and A. M. Läuchli, Universal signatures of quantum critical points from finite-size torus spectra: A window into the operator content of higher-dimensional conformal field theories, Phys. Rev. Lett. **117**, 210401 (2016).

[76] S. Whitsitt and S. Sachdev, Transition from the $\mathbb{Z}_2$ spin liquid to antiferromagnetic order: Spectrum on the torus, Phys. Rev. B **94**, 085134 (2016).

[77] S. Whitsitt, M. Schuler, L.-P. Henry, A. M. Läuchli, and S. Sachdev, Spectrum of the Wilson-Fisher conformal field theory on the torus, Phys. Rev. B **96**, 035142 (2017).

[78] M. Schuler, S. Hesselmann, S. Whitsitt, T. C. Lang, S. Wessel, and A. M. Läuchli, Torus spectroscopy of the Gross-Neveu-Yukawa quantum field theory: Free Dirac versus chiral Ising fixed point, Phys. Rev. B **103**, 125128 (2021).

[79] A. Wietek, S. Capponi, and A. M. Läuchli, Quantum electrodynamics in 2 + 1 dimensions as the organizing principle of a triangular lattice antiferromagnet, Phys. Rev. X **14**, 021010 (2024).

[80] S. Khatua, R. Shankar, and R. Ganesh, Quantum spin quadrumer, Phys. Rev. B **97**, 054403 (2018).

[81] S. Khatua, D. Sen, and R. Ganesh, Effective theories for quantum spin clusters: Geometric phases and state selection by singularity, Phys. Rev. B **100**, 134411 (2019).

[82] S. Khatua and R. Ganesh, Berry phase in the rigid rotor: Emergent physics of odd antiferromagnets, Phys. Rev. B **105**, 184401 (2022).

[83] C. E. Agrapidis, J. van den Brink, and S. Nishimoto, Ordered states in the Kitaev-Heisenberg model: From 1D chains to 2D honeycomb, Scientific Reports **8**, 1815 (2018).

[84] W. Yang, A. Nocera, and I. Affleck, Comprehensive study of the phase diagram of the spin-$\frac{1}{2}$ Kitaev-Heisenberg-Gamma chain, Phys. Rev. Res. **2**, 033268 (2020).

[85] A. Kitaev, Anyons in an exactly solved model and beyond, Annals of Physics **321**, 2 (2006).

[86] M. E. Zhitomirsky, M. V. Gvozdikova, P. C. W. Holdsworth, and R. Moessner, Quantum order by disorder and accidental soft mode in $Er_2Ti_2O_7$, Phys. Rev. Lett. **109**, 077204 (2012).

[87] J. G. Rau and M. J. P. Gingras, Frustrated quantum rare-earth pyrochlores, Annual Review of Condensed Matter Physics **10**, 357 (2019).

[88] V. S. Maryasin and M. E. Zhitomirsky, Order from structural disorder in the *XY* pyrochlore antiferromagnet $Er_2Ti_2O_7$, Phys. Rev. B **90**, 094412 (2014).

END MATTER

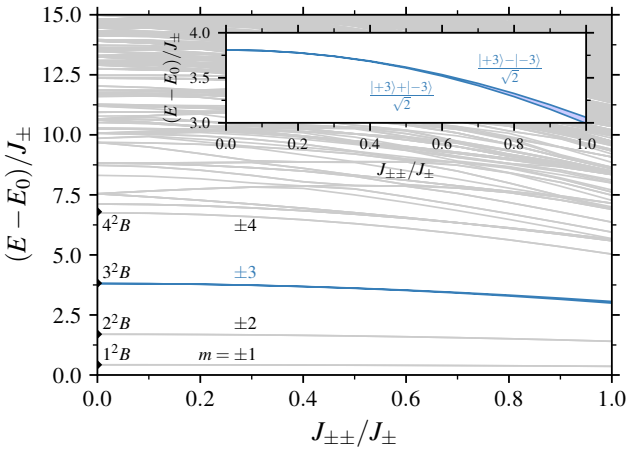

FIG. E1. Spectrum of a single cubic unit cell ($N = 16$) of the best fit model Eq. (E1) of $Er_2Ti_2O_7$ tuning away from the XY limit. Low-lying states form an approximate tower corresponding to a U(1) rotor with $(E - E_0)/J_\pm = m^2B$ where $m = 0, \pm1, \pm2, \ldots$ and $B \approx 0.4248$. (Inset) Splitting of the $m = \pm3$ levels into even and odd combinations $(|+3\rangle \pm |-3\rangle)/\sqrt{2}$ is a direct indicator of the ObQD strength.

Appendix A: Application to $Er_2Ti_2O_7$

As another non-trivial application of the above framework, we consider one of the best material examples of ObQD, $Er_2Ti_2O_7$ [30, 86]. The magnetic physics of this compound is described by an effective spin-$\frac{1}{2}$ model for the lowest-lying crystal field doublet of the Er^{3+} ion [87]. At nearest neighbor level symmetry constrains this to four independent exchanges [87]

$$\mathcal{H} \equiv \sum_{\langle ij \rangle} \Big[J_{zz} S_i^z S_j^z - J_\pm \left(S_i^+ S_j^- + S_i^- S_j^+ \right) + J_{\pm\pm} \left(\gamma_{ij} S_i^+ S_j^+ + \text{h.c.} \right) + J_{z\pm} \left(\zeta_{ij} \left[S_i^z S_j^+ + S_i^+ S_j^z \right] + \text{h.c.} \right) \Big]. \tag{E1}$$

Fitting to inelastic neutron scattering experiments yields the parameters [30]

$$J_{zz} = -0.025 \text{ meV}, \qquad J_\pm = +0.065 \text{ meV},$$
$$J_{\pm\pm} = +0.042 \text{ meV}, \qquad J_{z\pm} = -0.0088 \text{ meV}.$$

Classically, a ferromagnetic XY phase is stabilized, $\boldsymbol{S}_i \equiv S\,(\hat{\boldsymbol{x}} \cos\phi + \hat{\boldsymbol{y}} \sin\phi)$, with an accidental U(1) degeneracy in the angle ϕ. Quantum fluctuations lift this degeneracy and select the ψ_2 state, corresponding in this language to $\phi = 2\pi n/6$ with $n = 0, 1, \ldots, 5$ [30, 86]. The ObQD potential can be modeled as $V(\phi) = -g \cos(6\phi)$ due to the three-fold symmetry of the lattice [30].

To simplify our analysis we will consider a minimal version of this model with $J_{zz} = J_{z\pm} = 0$ and vary the ratio $J_{\pm\pm}/J_\pm$ [86]. We have performed full ED on single cubic unit cell of the pyrochlore lattice of $N = 16$ spins, exploiting translation invariance to reduce the block size. The spectrum as a function of $J_{\pm\pm}/J_\pm$ is shown in Fig. E1. The low lying states form an Anderson tower corresponding to a U(1) quantum rotor, with energy levels approximately given by $m^2BJ_\pm$ where m is an integer and $B \approx 0.4248$.

We can see that there is a very weak splitting in the third excited doublet, corresponding to mixing of the $m = \pm3$ states. Explicitly, we extend this as in the main text and construct a BLM model of the form

$$\mathcal{H}_{\text{eff}} = B(S^z_{\text{tot}})^2 - \frac{g}{2} \left\{ \frac{(S^+_{\text{tot}})^6 + (S^-_{\text{tot}})^6}{[N/2(N/2+1)]^3} \right\},$$

where $S^z = \sum_i S_i^z$ and $N = 16$. Following the same line of argument as the main text, we can extract the coefficient g directly from the splitting, with the splitting given as

$$\Delta_{\text{BLM}} = g \left\{ \frac{(N/2+3)(N/2+2)(N/2-1)(N/2-2)}{[N/2(N/2+1)]^2} \right\}.$$

For a sixteen site cluster this implies that $g \approx 1.122\Delta_{\text{BLM}}$. The value of g obtained using the splitting from ED spectrum as a function of $J_{\pm\pm}/J_\pm$ is shown in Fig. E2, alongside the value for g inferred from LSWT by comparison of the ZPEs of the ψ_2 and ψ_3 states [30].

Qualitative agreement is seen even for this small size, with the ED results larger than the LSWT by a factor of ≈ 2. Neglecting J_{zz} and $J_{z\pm}$ the best fit exchanges for $Er_2Ti_2O_7$ would fall at $J_{\pm\pm}/J_\pm \approx 0.646$ with $g_{\text{ED}} \approx 0.0875$ μeV and $g_{\text{LSWT}} \approx 0.0436$ μeV. These are comparable to the values extracted for the full set of exchanges, including J_{zz} and $J_{z\pm}$, which yields $g_{\text{ED}} \approx 0.0797$ μeV and $g_{\text{LSWT}} \approx 0.0423$ μeV.

We note that calculations based on a real-space perturbation theory (RSPT) approach [88] yields $g = SJ^3_{\pm\pm}/(192J^2_\pm)$ from the bare result and $g \approx 3J^3_{\pm\pm}/(2000J^2_{\pm\pm})$ from a resummation specifically at $S = 1/2$. These yield estimates $g_{\text{RSPT,bare}} \approx 0.046$ μeV and $g_{\text{RSPT,resum}} \approx 0.026$ μeV. That these estimates are comparable to ours may provide some insight into why we can obtain estimates for g from such small clusters, given the real space perturbation theory is inherently local and only involves a few neighboring sites.

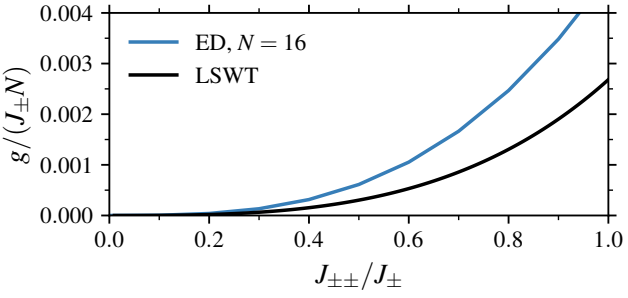

FIG. E2. Splitting of the $m = \pm3$ level in ED (see Fig. E1) yields the coefficient, g, in the ObQD selection energy $-g\cos(6\phi)$; corresponding semiclassical estimate from LSWT is shown.

Supplemental Material for "Finite-Size Spectral Signatures of Order by Quantum Disorder: A Perspective from Anderson's Tower of States"

Subhankar Khatua,[1,2,3] Griffin C. Howson,[1,2] Michel J. P. Gingras,[1,4] and Jeffrey G. Rau[2]

[1]*Department of Physics and Astronomy, University of Waterloo, Waterloo, Ontario, N2L 3G1, Canada*
[2]*Department of Physics, University of Windsor, 401 Sunset Avenue, Windsor, Ontario, N9B 3P4, Canada*
[3]*Institute for Theoretical Solid State Physics, IFW Dresden and Würzburg-Dresden Cluster of Excellence ct.qmat, Helmholtzstr. 20, 01069 Dresden, Germany*
[4]*Waterloo Institute for Nanotechnology, University of Waterloo, Waterloo, Ontario, N2L 3G1, Canada*

(Dated: September 12, 2025)

I. EFFECTIVE LIEB-MATTIS MODEL

To understand the mechanism of order by quantum disorder (ObQD) in a quantum spin-1/2 system, we develop an effective theory based on the Lieb-Mattis (LM) description which has previously been employed to investigate the finite-size signatures of spontaneous symmetry breaking [1–3]. The LM Hamiltonian can be obtained by projecting the full spin Hamiltonian onto its low-energy subspace [4, 5], $P\mathcal{H}P \equiv \mathcal{H}_{\rm LM}$, where P is the projector onto the subspace. This subspace can be determined by identifying the classical ordering pattern of the system's ground state or alternatively through the spin-spin correlation functions of the quantum ground state obtained via exact diagonalization (ED). For example, if the classical ground state ordering is ferromagnetic, the relevant subspace is the 'ferromagnetic' Hilbert space of total spin $S_{\rm tot} = N/2$ where N is the total number of $S = 1/2$ spins. Here, the projected Hamiltonian would involve a single "large" spin $S_{\rm tot}$ of length $N/2$, which can be solved exactly. For more complex orders involving multiple sublattices N_s, the projection needs to be onto the subspace of N_s large spins, each of length $\tilde{N}/2$, where $\tilde{N} = N/N_s$ is the number of spins in each sublattice. Ref. [4] outlines a straightforward way to perform these projections, making use of the fact that the projected Hamiltonian must be symmetric under any permutation of spins within a sublattice. To illustrate this procedure, consider a Hamiltonian term of the form, $S^\mu_{\boldsymbol{r}} S^\nu_{\boldsymbol{r}'}$ where $\boldsymbol{r}$, $\boldsymbol{r}'$ are lattice sites and $\mu, \nu = x, y, z$ denote components. The projection of this term can be achieved as follows –

Different sublattices.— If $\boldsymbol{r}$ and $\boldsymbol{r}'$ belong to two different sublattices, say, A and B respectively,

$$PS^\mu_{\boldsymbol{r}} S^\nu_{\boldsymbol{r}'} P = \frac{S^\mu_A S^\nu_B}{\tilde{N}^2}, \tag{S1}$$

where S^μ_A and S^ν_B are each of spin-length $\frac{\tilde{N}}{2}$.

Same sublattice.— To obtain the projection when $\boldsymbol{r}$ and $\boldsymbol{r}'$ belong to the same sublattice, e.g., A, we start from the relation

$$\begin{aligned} S^\mu_{A,\rm tot} S^\nu_{A,\rm tot} &= \sum_{\boldsymbol{r}\in A} S^\mu_{\boldsymbol{r}} S^\nu_{\boldsymbol{r}} + \sum_{\boldsymbol{r}\neq\boldsymbol{r}'\in A} S^\mu_{\boldsymbol{r}} S^\nu_{\boldsymbol{r}'} \\ &= \frac{\tilde{N}\delta_{\mu\nu}}{4} I + \frac{i\epsilon_{\mu\nu\sigma}}{2} S^\sigma_{A,\rm tot} + \sum_{\boldsymbol{r}\neq\boldsymbol{r}'\in A} S^\mu_{\boldsymbol{r}} S^\nu_{\boldsymbol{r}'}, \end{aligned} \tag{S2}$$

where $\boldsymbol{S}_{A,\rm tot} = \sum_{\boldsymbol{r}\in A} \boldsymbol{S}_{\boldsymbol{r}}$. In the last step in Eq. (S2), we have made use of the algebra of Pauli matrices and I is an identity matrix. From Eq. (S2), using spin permutation symmetry within this sublattice, we obtain

$$PS^\mu_{\boldsymbol{r}} S^\nu_{\boldsymbol{r}'} P = \frac{1}{\tilde{N}(\tilde{N}-1)} \left(S^\mu_A S^\nu_A - \frac{\tilde{N}\delta_{\mu\nu}}{4} I - \frac{i\epsilon_{\mu\nu\sigma}}{2} S^\sigma_A \right), \tag{S3}$$

where again S^μ_A is an emergent spin of length $\frac{\tilde{N}}{2}$. The denominator $\tilde{N}(\tilde{N}-1)$ arises from projecting the last term in Eq. (S2) which sums over all spin-spin interaction pairs within sublattice-A considering double counting, with $(\tilde{N}-1)$ pairs for each spin.

Eqs. (S1) and (S3) provide the necessary projections to derive the LM Hamiltonian, corresponding to the full microscopic Hamiltonian. A similar description may also be obtained using a semiclassical approach based on the spin path integral formalism [6–9].

II. HEISENBERG-COMPASS MODEL ON THE SQUARE LATTICE

A. Ferromagnetic regime

Derivation of the Lieb-Mattis Hamiltonian.— Here, we elaborate on the formalism for constructing the LM Hamiltonian of the Heisenberg compass model on the square-lattice. Although the Hamiltonian has already been introduced in the main text, we provide it again here for the convenience of discussion. The Hamiltonian is given by

$$\mathcal{H} = \sum_{\boldsymbol{r}} \Big[J \sum_{\delta=\boldsymbol{x},\boldsymbol{y}} \boldsymbol{S}_{\boldsymbol{r}} \cdot \boldsymbol{S}_{\boldsymbol{r}+\delta} + K \left(S^x_{\boldsymbol{r}} S^x_{\boldsymbol{r}+\boldsymbol{x}} + S^y_{\boldsymbol{r}} S^y_{\boldsymbol{r}+\boldsymbol{y}} \right) \Big], \tag{S4}$$

where $\boldsymbol{S}_{\boldsymbol{r}}$ represents a spin-1/2 operator at site $\boldsymbol{r}$ on the square lattice and $\delta = \boldsymbol{x}, \boldsymbol{y}$ refers to the nearest-neighbor bonds. We parametrize $J \equiv \cos\xi$ and $K \equiv \sin\xi$ with $\pi < \xi < 3\pi/2$, such that both couplings are ferromagnetic (i.e., negative). As discussed in the main text, the classical ground states are uniform fully polarized ferromagnetic configurations along arbitrary directions in the $\hat{\boldsymbol{x}} - \hat{\boldsymbol{y}}$ plane, given by

$$\boldsymbol{S}_{\boldsymbol{r}} = S\,(\cos\phi\,\hat{\boldsymbol{x}} + \sin\phi\,\hat{\boldsymbol{y}}), \tag{S5}$$

where $\phi \in [0, 2\pi)$ characterizes the orientation of the magnetization relative to the $\hat{\boldsymbol{x}}$ axis. Since the classical ground states are ferromagnetic, i.e., has one magnetic sublattice, as discussed in Sec. I, the relevant low-energy subspace is the space of $S_{\rm tot} = N/2$. Thus, to construct the LM Hamiltonian of this

model, we project the Hamiltonian in Eq. (S4) onto the sector $S_{\rm tot} = N/2$. Using Eq. (S3), we have

$$PS^{\mu}_{\boldsymbol{r}}S^{\mu}_{\boldsymbol{r}'}P = \frac{(S^{\mu}_{\rm tot})^2 - \frac{N}{4}I}{N(N-1)}, \tag{S6}$$

and finally the LM Hamiltonian of Eq. (S4) is:

$$\begin{aligned}\mathcal{H}_{\rm LM} &= \frac{2J[\boldsymbol{S}^2_{\rm tot} - \frac{3N}{4}I] + K\left((S^x_{\rm tot})^2 + (S^y_{\rm tot})^2 - \frac{N}{2}I\right)}{N-1} \\ &= \frac{2J[\boldsymbol{S}^2_{\rm tot} - \frac{3N}{4}I] + K\left(\boldsymbol{S}^2_{\rm tot} - (S^z_{\rm tot})^2 - \frac{N}{2}I\right)}{N-1}.\end{aligned} \tag{S7}$$

In the sector $S_{\rm tot} = N/2$, $\boldsymbol{S}^2_{\rm tot}$ is proportional to the identity operator. Ignoring all terms that are proportional to the identity operator, we have

$$\mathcal{H}_{\rm LM} = -\frac{K}{(N-1)}(S^z_{\rm tot})^2. \tag{S8}$$

This describes a planar rotor. Its spectrum is discussed in the main text and begins to capture some qualitative features of the ED data [see the main text for more details]. We reiterate here that this Hamiltonian has a U(1) symmetry, a consequence of the classical accidental degeneracy of the parent Hamiltonian [Eq. (S4)], and thus, does not exhibit ObQD. We must go beyond the LM description to be able to capture ObQD.

Derivation of the Beyond Lieb-Mattis Hamiltonian.— As discussed in the main text, to investigate the effects of ObQD, we add an additional term to the LM Hamiltonian [Eq. (S8)] corresponding to the spin-wave zero-point energy (ZPE). The ZPE in this model is of the form $-g\cos(4\phi)$ [10] where, g denotes the ObQD energy scale. We will now rewrite this term in such a way that can be easily promoted to the operator form in the $S_{\rm tot} = N/2$ subspace. The components of the total spin in the classical ground states are $S^x_{\rm tot} = \frac{N}{2}\cos\phi$ and $S^y_{\rm tot} = \frac{N}{2}\sin\phi$, giving $S^+_{\rm tot} \equiv \left(S^x_{\rm tot} + iS^y_{\rm tot}\right) = \frac{N}{2}\exp(i\phi)$ and $S^-_{\rm tot} \equiv \left(S^x_{\rm tot} - iS^y_{\rm tot}\right) = \frac{N}{2}\exp(-i\phi)$. Thus, in terms of the total classical spin, the ZPE may be written as

$$-g\cos(4\phi) = -\frac{g}{2}\frac{(S^+_{\rm tot})^4 + (S^-_{\rm tot})^4}{(N/2)^4}. \tag{S9}$$

Therefore, the minimal term that needs to be added to Eq. (S8) to take into account ObQD is the operator equivalent of Eq. (S9), which is

$$-\frac{g}{2}\frac{(S^+_{\rm tot})^4 + (S^-_{\rm tot})^4}{[N/2\,(N/2+1)]^2}, \tag{S10}$$

where $S^+_{\rm tot}$ refers to the raising operator in the $S_{\rm tot} = N/2$ subspace and we have modified $(N/2)^2 \to N/2(N/2+1)$ to account for the classical to quantum spin-length conversion. Note that this replacement is a phenomenological or ad hoc normalization. The precise N-dependence could in principle be derived from higher-order many-body perturbation theory. However, this is computationally challenging for anisotropic Hamiltonians [11]. Nevertheless, the qualitative physics remains unaffected by the exact normalization. In our phenomenological effective description, we adopt $N/2(N/2+1)$ to reflect naturally the quantum analog of spin-length of the effective large spin. With this, the beyond Lieb-Mattis (BLM) model of the ferromagnetic Heisenberg-compass model on the square lattice is given by

$$\mathcal{H}_{\rm BLM} = \mathcal{H}_{\rm LM} - \frac{g}{2}\frac{(S^+_{\rm tot})^4 + (S^-_{\rm tot})^4}{[N/2(N/2+1)]^2}. \tag{S11}$$

Note that ZPE is an extensive quantity (i.e., $\propto N$), thus $g \propto N$. Thus, for a 4×4 square lattice, g is quite small and therefore, the additional term in Eq. (S11) behaves as a perturbation to the bare LM Hamiltonian, modifying the bare spectrum of Eq. (S8) slightly. Identifying

$$\mathcal{H}_{\rm pert} \equiv -\frac{g}{2}\frac{(S^+_{\rm tot})^4 + (S^-_{\rm tot})^4}{[N/2(N/2+1)]^2}, \tag{S12}$$

this perturbation will split the degenerate $m = \pm 2$ states of the bare LM Hamiltonian at the first order. To see this explicitly, we construct the perturbation matrix on the $m = \pm 2$ space

$$\boldsymbol{W} \equiv \begin{bmatrix} \langle -2|\mathcal{H}_{\rm pert}|-2\rangle & \langle -2|\mathcal{H}_{\rm pert}|+2\rangle \\ \langle +2|\mathcal{H}_{\rm pert}|-2\rangle & \langle +2|\mathcal{H}_{\rm pert}|+2\rangle \end{bmatrix}, \tag{S13}$$

where the diagonal terms are zero as can be seen from the form of the perturbation. The off-diagonal term is given by

$$\begin{aligned}\langle -2|\mathcal{H}_{\rm pert}|+2\rangle &= -\frac{g\langle -2|[(S^+_{\rm tot})^4 + (S^-_{\rm tot})^4]|+2\rangle}{2\,[N/2(N/2+1)]^2} \\ &= -\frac{g\langle -2|(S^-_{\rm tot})^4|+2\rangle}{2[N/2(N/2+1)]^2} \\ &= -\frac{g(N/2-1)(N/2+2)}{N(N/2+1)},\end{aligned} \tag{S14}$$

and $\langle +2|\mathcal{H}_{\rm pert}|-2\rangle = \langle -2|\mathcal{H}_{\rm pert}|+2\rangle = -\frac{g(N/2-1)(N/2+2)}{N(N/2+1)}$. The eigenvalues of $\boldsymbol{W}$ are $\pm\frac{g(N/2-1)(N/2+2)}{N(N/2+1)}$ and thus, the splitting of the $m = \pm 2$ states under the perturbation $\mathcal{H}_{\rm pert}$ is $\Delta = \frac{2g(N/2-1)(N/2+2)}{N(N/2+1)}$. We equate this Δ with the splitting observed in ED to get an estimate of the ObQD energy scale g from ED. That is, we take

$$g = \frac{N/2(N/2+1)}{(N/2-1)(N/2+2)}\Delta_{\rm ED}, \tag{S15}$$

where $\Delta_{\rm ED}$ is the splitting obtained from ED. A comparison of g obtained from ED to that obtained from LSWT on the N-site square-lattice is provided in the main text.

B. Antiferromagnetic regime

We extend our study of the Heisenberg-compass model on the square lattice to the antiferromagnetic regime ($0 < \xi < \pi/2$) where $J > 0, K > 0$. The classical ground states in this

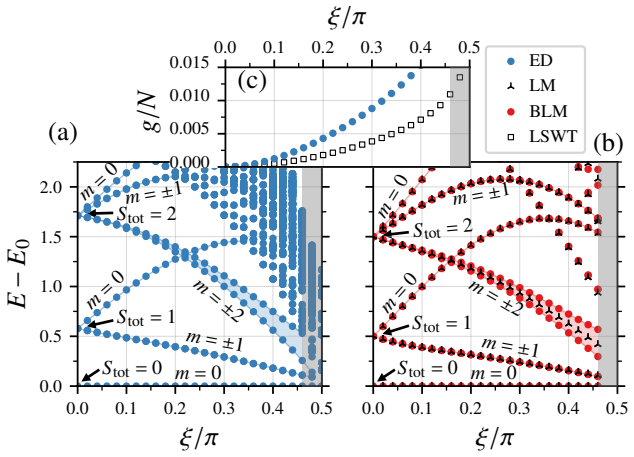

FIG. S1. Antiferromagnetic Heisenberg-compass model on the square lattice of $N = 16$ sites with periodic boundary conditions. (a) Low-energy ED spectrum. (b) Spectrum of the corresponding LM and BLM models. The value of g in the BLM model is extracted from the splitting in the ED spectrum. (c) Comparison of g obtained from LSWT and ED spectrum. Grey areas in all panels mark the regime where the low-energy physics deviates from the BLM picture because of a new state appearing in the microscopic model at $\xi = \pi/2$ [10].

regime are accidentally degenerate Néel states with arbitrary Néel-vector orientation in the $\hat{\boldsymbol{x}} - \hat{\boldsymbol{y}}$ plane [10], described by

$$\boldsymbol{S}_{\boldsymbol{r}} = (-1)^r S\,(\cos\phi\,\hat{\boldsymbol{x}} + \sin\phi\,\hat{\boldsymbol{y}})\,, \tag{S16}$$

where $\phi \in [0, 2\pi)$ characterizes the orientation of the staggered magnetization relative to the $\hat{\boldsymbol{x}}$ axis. Similar to the ferromagnetic regime, the accidentally degenerate ground states form an O(2) manifold. The occurrence of ObQD in this regime has been demonstrated in Ref. [10] using spin-wave theory, which selects the Néel states along $\pm\hat{\boldsymbol{x}}, \pm\hat{\boldsymbol{y}}$ directions.

To probe the signatures of ObQD in this antiferromagnetic regime in the spin-1/2 limit, we perform ED exploiting the same symmetry (i.e., discrete translation symmetry of the model) as done in the ferromagnetic regime. The resulting ED spectrum is shown in Fig. S1(a). To identify which features in this spectrum arise from ObQD, we follow the same effective BLM model construction as introduced for the ferromagnetic regime. To this end, we first derive the corresponding LM Hamiltonian. Unlike the ferromagnetic ground states in the ferromagnetic regime, here we have Néel states—two sublattices (A and B) in the unit cell. Thus, as explained in Sec. I, the LM model comes from projecting the full Hamiltonian onto the subspace formed by two large spins $S_A = \tilde{N}/2 = N/4$ and $S_B = N/4$. Using Eq. (S1) on Eq. (S4), we have

$$\begin{aligned}\mathcal{H}_{\rm LM} &= \frac{8JS\boldsymbol{S}_A \cdot \boldsymbol{S}_B + 4K\left(S_A^x S_B^x + S_A^y S_B^y\right)}{N} \\ &= \frac{4J + 2K}{N}(\boldsymbol{S}_{\rm tot}^2 - \boldsymbol{S}_A^2 - \boldsymbol{S}_B^2) - \frac{4K}{N} S_A^z S_B^z,\end{aligned} \tag{S17}$$

where $\boldsymbol{S}_{\rm tot} \equiv \boldsymbol{S}_A + \boldsymbol{S}_B$ (sum of two $N/4$-length spins). For this $\mathcal{H}_{\rm LM}$, while $S_{\rm tot}$ is not a good quantum number, $S_{\rm tot}^z$ is. Fig. S1(b) shows the LM spectrum with m denoting the eigenvalues of $S_{\rm tot}^z$. At $\xi = 0$, the model reduces to the isotropic Heisenberg antiferromagnet (HAF) on the square lattice which enjoys a true SU(2) symmetry, and thus $S_{\rm tot}$ is conserved too, labeled in Fig. S1(b). As ξ is varied from zero to introduce finite compass interactions, the $m = 0$ state [adiabatically connected to $S_{\rm tot} = 1$] and $m = \pm 2$ states [connected to $S_{\rm tot} = 2$] cross at $\xi \sim 0.16\pi$ without mixing due to their distinct m values. The LM spectrum shows good qualitative agreement with the low-energy ED spectrum of the full Hamiltonian, as displayed in Fig. S1(a). However, the splitting of $m = \pm 2$ states observed in the ED spectrum is *absent* in the LM spectrum. This has to do with the U(1) symmetry of $\mathcal{H}_{\rm LM}$, reflecting the accidental degeneracy in the ground states—thus failing to capture ObQD.

As in the case of the ferromagnetic regime [Sec. II A], $\mathcal{H}_{\rm LM}$ must be augmented by the operator corresponding to the spin-wave ZPE to obtain the BLM Hamiltonian. The ZPE takes the form $-g\cos(4\phi)$ with four minima [$\phi = 0, \pi/2, \pi, 3\pi/2$] corresponding to the four Néel configurations along the $\pm\hat{\boldsymbol{x}}, \pm\hat{\boldsymbol{y}}$ directions [10]. The components of the staggered magnetization in the ground states, $n_{\rm tot}^x = S_A^x - S_B^x = \frac{N}{2}\cos\phi$ and $n_{\rm tot}^y = S_A^y - S_B^y = \frac{N}{2}\sin\phi$, giving $n_{\rm tot}^+ \equiv \left(n_{\rm tot}^x + i n_{\rm tot}^y\right) = \frac{N}{2}\exp(i\phi)$ and $n_{\rm tot}^- \equiv \left(n_{\rm tot}^x - i n_{\rm tot}^y\right) = \frac{N}{2}\exp(-i\phi)$. Thus, in terms of the staggered magnetization, the ZPE is $-(g/2)\left[(n_{\rm tot}^+)^4 + (n_{\rm tot}^-)^4\right]/(N/2)^4$. Therefore, the minimal term that needs to be added to Eq. (S17) to take into account ObQD is

$$-\frac{g}{2}\frac{\left[(n_{\rm tot}^+)^4 + (n_{\rm tot}^-)^4\right]}{2^4\left[\frac{N}{4}(\frac{N}{4}+1)\right]^2}, \tag{S18}$$

where we have shifted $(N/4)^2 \to (N/4)(N/4+1)$ to account for the conversion of classical to quantum spin-length corresponding to each sublattice A and B. Thus, the BLM model for the antiferromagnetic Heisenberg-compass model on the square lattice is given by

$$\mathcal{H}_{\rm BLM} \equiv \mathcal{H}_{\rm LM} - \frac{g}{2}\frac{(S_A^+ - S_B^+)^4 + (S_A^- - S_B^-)^4}{[N/2(N/2+2)]^2}, \tag{S19}$$

This added term behaves as a perturbation on $\mathcal{H}_{\rm LM}$ since g is weaker for smaller systems. First-order in this perturbation changes S_A^z and S_B^z in such a way that the states satisfying $\Delta m = \pm 4$ split, thus we expect splitting of the $m = \pm 2$ level. To extract the g value from the splitting of the $m = \pm 2$ in the ED spectrum, we compute the first-order perturbation splitting within the BLM description numerically with g as an undetermined multiplicative parameter, and then equate it to the splitting in ED. We find an overall good agreement between the BLM and ED spectra using this extracted value, as shown in Fig. S1(b). Fig. S1(c) shows a comparison of the g obtained from LSWT and from the splitting of $m = \pm 2$ states in the ED spectrum, differing only roughly by a factor of two.

III. HEISENBERG-KITAEV MODEL ON THE HONEYCOMB LATTICE

A. Antiferromagnetic regime

Heisenberg-Kitaev model on the honeycomb lattice in the antiferromagnetic regime has been discussed in the main text. Here, we provide the details of the derivations of the corresponding LM and BLM Hamiltonians. The model is described by the Hamiltonian

$$\mathcal{H} = \sum_{\langle \boldsymbol{r}\boldsymbol{r}'\rangle_\gamma} \left[J\boldsymbol{S}_{\boldsymbol{r}} \cdot \boldsymbol{S}_{\boldsymbol{r}'} + KS^\gamma_{\boldsymbol{r}} S^\gamma_{\boldsymbol{r}'} \right], \tag{S20}$$

where J, K are the Heisenberg and Kitaev couplings, respectively, and $\gamma = x, y, z$ refer to both spin components and the three distinct nearest-neighbor bonds. This model possesses discrete rotation symmetries like C_3 about the axis perpendicular to the lattice plane, C_2 about the bond directions, and spin-only C_2 rotations about $\hat{\boldsymbol{x}}, \hat{\boldsymbol{y}}, \hat{\boldsymbol{z}}$ directions. We take $J \equiv \cos\xi$ and $K \equiv \sin\xi$ with $0 < \xi < \pi/2$, such that both couplings are antiferromagnetic. As discussed in the main text, the classical ground states are accidentally degenerate Néel states with Néel vector oriented along any arbitrary direction and ObQD selects only those along the cubic axes (i.e., $\pm\hat{\boldsymbol{x}}$, $\pm\hat{\boldsymbol{y}}$, $\pm\hat{\boldsymbol{z}}$) [12–14]. Since the classical ground state is a Néel order, the LM Hamiltonian can be obtained by projecting Eq. (S20) onto the subspace spanned by two spins S_A and S_B of length $N/4$, exactly as done for the antiferromagnetic Heisenberg-compass model in Sec. II B. Using the projection in Eq. (S1) on the full Hamiltonian [Eq. (S20)], we obtain

$$\mathcal{H}_{\rm LM} = \frac{3J+K}{N}(\boldsymbol{S}^2_{\rm tot} - \boldsymbol{S}^2_A - \boldsymbol{S}^2_B). \tag{S21}$$

In this case, the LM Hamiltonian exhibits an augmented SU(2) symmetry, thus resulting in both $S_{\rm tot}$ and $S^z_{\rm tot}$ as good quantum numbers. The spectrum of Eq. (S21) is discussed in the main text.

To include ObQD in the effective description, the LM Hamiltonian needs to be augmented by the operator equivalent of the spin-wave ZPE. The ZPE minimizes for the Néel states with Néel-vector along the cubic axes [12–14], taking the form of the cubic anisotropy on the ground state manifold. This can be written as an operator in the two-spin subspace as

$$-g\frac{[(S^x_A - S^x_B)^4 + (S^y_A - S^y_B)^4 + (S^z_A - S^z_B)^4]}{[N/4(N/4+1)]^2}. \tag{S22}$$

This cubic anisotropy term breaks the SU(2) symmetry of $\mathcal{H}_{\rm LM}$, which was accidental for the full model [Eq. (S20)], and restores all the discrete symmetries as mentioned above. For smaller systems, this term acts as a perturbation on $\mathcal{H}_{\rm LM}$, analogous to the cubic crystal electric field effect on a SU(2) symmetric magnetic single ion. This splits the $S_{\rm tot} = 2$ and higher energy levels of $\mathcal{H}_{\rm LM}$. The level $S_{\rm tot} = 2$ splits into the spin-analog of an orbital e_g doublet and t_{2g} triplet [15]. This splitting is also observed in the ED spectrum. To determine g from this splitting in ED, we numerically find the first-order perturbation spitting of $S_{\rm tot} = 2$ states within BLM picture due to the perturbation in Eq. (S22) with g as an undetermined multiplicative factor and equate this splitting to that from ED. The comparison of g obtained from the splitting in ED spectrum and LSWT has been presented in the main text.

In principle, one can further understand the splitting of the $S_{\rm tot} = 3$ level within this description. However, these states are difficult to identify in ED spectrum due to level crossings with high energy non-rotor states which intrude above the $S_{\rm tot} = 2$ level.

B. Ferromagnetic regime

We move on now to consider the ferromagnetic regime with $\pi < \xi < 3\pi/2$ such that $J < 0, K < 0$. In contrast to the antiferromagnetic regime, the classical ground states in this regime are fully polarized ferromagnetic states pointing along any arbitrary direction, with ObQD selecting only those aligned along the cubic axes (i.e., $\pm\hat{\boldsymbol{x}}, \pm\hat{\boldsymbol{y}}, \pm\hat{\boldsymbol{z}}$), as shown using spin-wave theory [12–14]. We next perform ED, and the resulting spectrum is shown in Fig. S2(a). To identify the characteristic splittings induced by ObQD in the ED spectrum, we construct the corresponding BLM Hamiltonian, following the same approach as in the previous examples. Since the classical ground state manifold is ferromagnetic, the projection involved in the effective description needs to be done on the space of single spin of length $S_{\rm tot} = N/2$, as done previously for the ferromagnetic Heisenberg-compass model on the square lattice. Making use of the projections derived for the ferromagnetic Heisenberg-compass model [Eq. (S6)] and omitting additive constants, we obtain

$$\mathcal{H}_{\rm LM} = \frac{3J+K}{2(N-1)}\boldsymbol{S}^2_{\rm tot}. \tag{S23}$$

As in the antiferromagnetic regime, the LM Hamiltonian exhibits an enhanced SU(2) symmetry, meaning both $S_{\rm tot}$ and $S^z_{\rm tot}$ are good quantum numbers. All the different $S^z_{\rm tot}$ states within the $S_{\rm tot} = N/2$ subspace are degenerate. Consequently, the LM model energy eigenvalues, when shifted by the ground state energy E_0, are all zero, i.e., $E - E_0 = 0$ for each ξ. For this reason, we do not show the LM spectrum in Fig. S2.

To break the SU(2) symmetry of the LM Hamiltonian down to the discrete symmetries of the full model, we next consider the spin-wave ZPE. This ZPE acts as a cubic anisotropy on the classical ground state manifold [12–14], yielding the following operator in the $S_{\rm tot} = N/2$ space

$$-g\frac{(S^x_{\rm tot})^4 + (S^y_{\rm tot})^4 + (S^z_{\rm tot})^4}{(N/2(N/2+1))^2}. \tag{S24}$$

This poses a cubic crystal field problem on the $S_{\rm tot} = N/2$ manifold rather than on the $S_{\rm tot} = 2$ manifold in the antiferromagnetic regime. To estimate g from ED, we use the splitting marked in light blue in the ED spectrum in Fig. S2(a). We numerically find the first-order perturbation (corresponding) splitting within the BLM model with g as an undetermined multiplicative parameter and equate it to the splitting in the

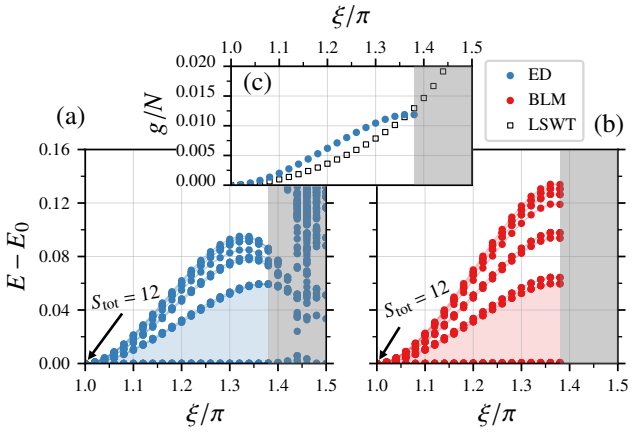

FIG. S2. Ferromagnetic Heisenberg-Kitaev model on the honeycomb lattice of $N = 24$ sites with periodic boundary conditions. (a) Low-energy ED spectrum. (b) BLM model spectrum. The g value in BLM description is determined from the splitting in the ED spectrum. (c) g obtained from LSWT and ED spectrum. Grey areas in all panels mark the regime where the low-energy physics deviates from the BLM description.

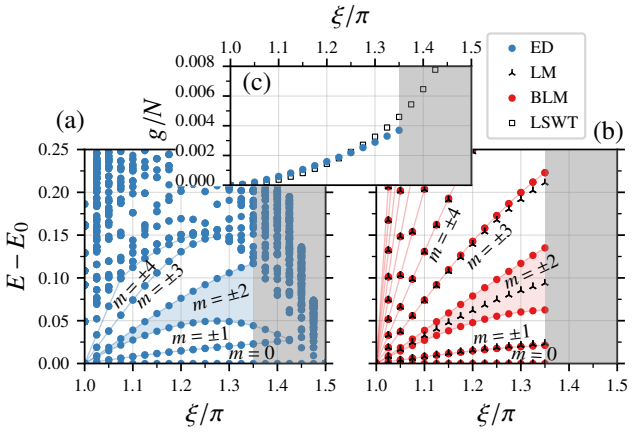

FIG. S3. Ferromagnetic Heisenberg-Kitaev spin chain of $N = 20$ sites with periodic boundary conditions. (a) Low-energy ED spectrum. (b) The LM and BLM model spectra. The g value for the BLM model is determined from the splitting in the ED spectrum. (c) Comparison of g obtained from LSWT and splitting in the ED spectrum. Grey-shaded regions in all panels indicate the regime where the low-energy physics deviates from the BLM description as it approaches a different phase in $1.44\pi \lesssim \xi \lesssim 1.5\pi$ [16].

ED spectrum, yielding an estimate for g from ED. Upon numerically diagonalizing the BLM Hamiltonian with these values of g, we observe that the cubic anisotropy term lifts the degeneracy of the $S_{\rm tot} = N/2$ multiplet, as seen in the BLM spectrum in Fig. S2(b), following the same degeneracy pattern of the split states in the ED spectrum [Fig. S2(a)]. We note good agreement between g obtained from ED and that obtained from LSWT, depicted in Fig. S2(c). However, this agreement breaks down in the range $1.38\pi \lesssim \xi \lesssim 1.5\pi$ (grey shaded region in Fig. S2), possibly due to the onset of Kitaev spin liquid physics around $\xi \sim 3\pi/2$, where the BLM description is no longer valid.

IV. HEISENBERG-KITAEV MODEL ON THE CHAIN

To round out our discussion of two- and three-dimensional systems explored in the main text, we present here results for a one-dimensional version of the ferromagnetic Heisenberg-Kitaev model, namely, the Heisenberg-Kitaev spin chain, known for its potential in providing insights into two-dimensional Kitaev physics [16–19]. It is governed by the Hamiltonian

$$\mathcal{H} = J \sum_{i=1}^{N} \boldsymbol{S}_i \cdot \boldsymbol{S}_{i+1} + K \sum_{i}^{N/2} \left(S^x_{2i-1} S^x_{2i} + S^y_{2i} S^y_{2i+1} \right), \quad \text{(S25)}$$

where i refers to the sites on the chain, and $J \equiv \cos\xi$, $K \equiv \sin\xi$ with $\pi < \xi < 3\pi/2$. The second term in Eq. (S25) corresponds to alternating $x-x$ and $y-y$ Kitaev couplings. The Kitaev term breaks continuous spin-rotation symmetry, leaving only discrete symmetries, such as a $\pi/2$ spin rotation about $\hat{\boldsymbol{z}}$ axis combined with unit lattice translation. Classical ground states are accidentally degenerate ferromagnetic configurations pointing along any arbitrary direction in the $\hat{\boldsymbol{x}} - \hat{\boldsymbol{y}}$ plane, with ObQD selecting only those aligned along $\pm\hat{\boldsymbol{x}}, \pm\hat{\boldsymbol{y}}$ directions. This is confirmed by analyzing the properties of the ground state using density matrix renormalization group (DMRG) method, although in $\pi < \xi \lesssim 1.44\pi$ [16]. For $1.44\pi \lesssim \xi \lesssim 1.5\pi$, a different phase emerges.

The ED spectrum, obtained using the combined lattice translational and spin-rotational symmetry mentioned above, is presented in Fig. S3(a). To identify the splittings due to ObQD, we next construct the effective description. Using the same projections as those employed for the ferromagnetic Heisenberg-compass model on the square lattice [Sec. II A], and omitting the constant terms, we obtain

$$\mathcal{H}_{\rm LM} = -\frac{K}{2(N-1)} (S^z_{\rm tot})^2. \quad \text{(S26)}$$

This Hamiltonian is the same as that for the ferromagnetic Heisenberg-compass model on the square lattice, except the prefactor. Therefore, their spectra are similar, as can be seen in Fig. S3(b). Since the spin-wave ZPE is minimized by ferromagnetic ground states aligned along $\pm\hat{\boldsymbol{x}}$ and $\pm\hat{\boldsymbol{y}}$, it takes the same form, $-g\cos 4\phi$, as in the ferromagnetic Heisenberg-compass model. Therefore, following the same reasoning, we obtain the ObQD-induced perturbation term

$$\mathcal{H}_{\rm pert} = -\frac{g}{2} \frac{(S^+_{\rm tot})^4 + (S^-_{\rm tot})^4}{\left[N/2(N/2+1)\right]^2}. \quad \text{(S27)}$$

This perturbation splits the $m = \pm 2$ states at first order in perturbation theory, and comparing this with the corresponding splitting from the ED spectrum, we can get an estimate of g from ED following the steps in Sec. II A as

$$g = \frac{N/2(N/2+1)}{(N/2-1)(N/2+2)} \Delta_{\rm ED}. \quad \text{(S28)}$$

The g value obtained from the ED data agrees quite well with the value derived from LSWT, as shown in Fig. S3(c). Comparing the BLM spectrum with the values of g found from ED [Fig. S3(b)] with the low-energy ED spectrum shown in Fig. S3(a) yields good qualitative agreement. Significant disagreement near $\xi \sim 3\pi/2$ arises due to the existence of a different phase in $1.44\pi \lesssim \xi \lesssim 1.5\pi$ [16], making the effective description inapplicable. While the agreement between ED and the effective model spectra is qualitatively good in this one-dimensional example, it is not as good as in the two- and three-dimensional cases. This is likely due to the enhanced quantum fluctuations that are intrinsic to one-dimensional systems, in contrast to their higher-dimensional counterparts.

[1] E. Lieb and D. Mattis, Ordering energy levels of interacting spin systems, Journal of Mathematical Physics **3**, 749 (1962).

[2] C. Lhuillier, Frustrated quantum magnets (2005), arXiv:cond-mat/0502464 [cond-mat.str-el].

[3] A. Wietek, M. Schuler, and A. M. Läuchli, Studying continuous symmetry breaking using energy level spectroscopy (2017), arXiv:1704.08622 [cond-mat.str-el].

[4] N.-G. Zhang, C. L. Henley, C. Rischel, and K. Lefmann, Effective Hamiltonian and low-lying eigenenergy clustering patterns of four-sublattice antiferromagnets, Phys. Rev. B **65**, 064427 (2002).

[5] T. Roscilde, T. Comparin, and F. Mezzacapo, Rotor/spin-wave theory for quantum spin models with u(1) symmetry, Phys. Rev. B **108**, 155130 (2023).

[6] S. Khatua, R. Shankar, and R. Ganesh, Quantum spin quadrumer, Phys. Rev. B **97**, 054403 (2018).

[7] S. Khatua, D. Sen, and R. Ganesh, Effective theories for quantum spin clusters: Geometric phases and state selection by singularity, Phys. Rev. B **100**, 134411 (2019).

[8] S. Khatua, S. Srinivasan, and R. Ganesh, State selection in frustrated magnets, Phys. Rev. B **103**, 174412 (2021).

[9] S. Khatua and R. Ganesh, Berry phase in the rigid rotor: Emergent physics of odd antiferromagnets, Phys. Rev. B **105**, 184401 (2022).

[10] S. Khatua, G. C. Howson, M. J. P. Gingras, and J. G. Rau, Ground state properties of the Heisenberg-compass model on the square lattice, Phys. Rev. B **110**, 104426 (2024).

[11] E. Liviotti, S. Carretta, and G. Amoretti, S-mixing contributions to the high-order anisotropy terms in the effective spin Hamiltonian for magnetic clusters, The Journal of Chemical Physics **117**, 3361 (2002).

[12] J. G. Rau, P. A. McClarty, and R. Moessner, Pseudo-Goldstone gaps and order-by-quantum disorder in frustrated magnets, Phys. Rev. Lett. **121**, 237201 (2018).

[13] J. Chaloupka, G. Jackeli, and G. Khaliullin, Kitaev-Heisenberg model on a honeycomb lattice: Possible exotic phases in iridium oxides A_2IrO_3, Phys. Rev. Lett. **105**, 027204 (2010).

[14] J. Chaloupka, G. Jackeli, and G. Khaliullin, Zigzag magnetic order in the iridium oxide Na_2IrO_3, Phys. Rev. Lett. **110**, 097204 (2013).

[15] P. Fazekas, *Lecture Notes on Electron Correlation and Magnetism* (World Scientific, New Jersey, 1999).

[16] W. Yang, C. Xu, S. Ma, A. Nocera, and I. Affleck, Left-left-right-right magnetic order in spin-$\frac{1}{2}$ Kitaev-Heisenberg chain, Phys. Rev. B **112**, 035104 (2025).

[17] C. E. Agrapidis, J. van den Brink, and S. Nishimoto, Ordered states in the Kitaev-Heisenberg model: From 1D chains to 2D honeycomb, Scientific Reports **8**, 1815 (2018).

[18] W. Yang, A. Nocera, and I. Affleck, Comprehensive study of the phase diagram of the spin-$\frac{1}{2}$ Kitaev-Heisenberg-Gamma chain, Phys. Rev. Res. **2**, 033268 (2020).

[19] A. Kitaev, Anyons in an exactly solved model and beyond, Annals of Physics **321**, 2 (2006).